

Nonclassical kinetics of an elementary $A+B\rightarrow C$ reaction-diffusion system showing effects of a speckled initial reactant distribution and eventual self-segregation: Experiments

Eric Monson and Raoul Kopelman

Departments of Chemistry, Physics and Applied Physics, University of Michigan, Ann Arbor, Michigan 48109, USA

(Received 21 May 2003; published 19 February 2004)

We demonstrate here the implementation of an experimental system suitable for the study of the diffusion limited $A+B\rightarrow 0$, nonclassical reaction behavior. Using a combination of a fluorescent calcium indicator and a calcium ion which is initially “caged,” a pulse of near-UV light initiates the reaction which is followed as product formation vs time. Sensitive dependence on the initial reactant distribution is observed through patterns in the uncaging UV light profile. In one case, the reaction progress passes through two nonclassical time regimes, one due to roughness originating from laser speckles, followed by one consistent with the three-dimensional Zeldovich rate of $(1/\rho_A - 1/\rho_{A0}) \sim t^{3/4}$, with features matching Monte Carlo simulations on this initial distribution. This behavior is contrasted with reactions initiated by a homogenous source which induces random initial reactant distributions, though both systems seem to approach the asymptotic limit of self-segregation of reactants.

DOI: 10.1103/PhysRevE.69.021103

PACS number(s): 05.40.-a, 82.20.-w

I. INTRODUCTION

For the simplest case of an elementary, irreversible, diffusion-limited reaction, $A+B\rightarrow C$, the generally accepted scaling law is

$$(1/\rho - 1/\rho_0) \sim t^\alpha, \quad \rho = \rho_A = \rho_B, \quad (1)$$

where $(1/\rho - 1/\rho_0)$ will be referred to as the *reaction progress*, and ρ_0 is the reactant density for both reactants ($\rho_A = \rho_B$) at $t=0$. Classical textbooks, from chemistry to solid-state physics [1], give $\alpha=1$. Nonclassical kinetics [2] gives the asymptotic ($t\rightarrow\infty$) relations

$$\alpha = d/4, \quad d \leq 4 \quad (2)$$

$$\alpha = 1, \quad d \geq 4, \quad (3)$$

for initially random distributions (the most widely studied case), irrespective of initial ρ [3,4]. We note that the nonclassical effects we deal with result from the preservation of a “memory” of the initial spatial reactant distribution, which isn’t limited to any certain concentration range. (Classical behavior requires thorough continuous stirring, i.e., rerandomization.)

While much theoretical work has been done on the initially random and geminate [5] reaction systems, only recently has consideration been given to other initially correlated systems. The theoretical work by Lindenberg and co-workers [6,7] showed the dramatic effects of varying $t=0$ spatial correlations in the $A+B\rightarrow 0$ system, resulting in a hierarchy of *reaction progress* time regimes, each with a different scaling law. For example, in the case of a fractal initial distribution [7], where the particles are landed on a one-dimensional lattice in a fractal pattern, a very slow reaction rate is observed due to the overabundance of long wavelength components in the spatial fluctuations of the reactant distribution (compared to the flat distribution of a random system).

Before this work, there has been no experimental verification of these nonclassical results. Furthermore, we believe that all experimental verifications of the classical result ($\alpha = 1$) involved stirred (i.e., constantly rerandomized) systems [8]. However, most real-life applications, from catalysis to geochemistry to biochemistry, do not allow stirring. For instance, much of the solid state and surface science literature still uses the classical formalism, e.g., exciton annihilation is assumed to be proportional to the square of the exciton density, or the rate of electron-hole recombination is assumed to be linear in both electron and hole densities [1]. We thus felt the need for some controlled experiments (where there is no convection or stirring) aimed at observing nonclassical behavior in an elementary $A+B$ reaction.

Besides our earlier reports [9,10], there have been no previous experimental studies on nongeminate initially correlated systems. In the work described here, a hierarchy of kinetic behaviors has indeed been observed for a simple, elementary, binary reaction, and two sets of initial conditions are tested with contrasting kinetics.

Although analytic and simulation work on these systems has been extensive, many practical barriers have contributed to the lack of experimental study. As in many areas of research, the challenge is not in finding a system in which the behaviors occur, but in finding a system which is sufficiently “clean” (i.e., one in which the behaviors under study are not masked by other complicating processes). The main $A+B\rightarrow C$ case which has been experimentally studied is that of initially separated reactants [11–13], and this has been quite fruitful in terms of the theoretical-experimental feedback loop. Other cases of initially more mixed reactants run into various difficulties. If the reaction is really diffusion limited, it will proceed very quickly at reasonable (i.e., detectable) reactant concentrations, so it becomes difficult to mix the components to a known distribution, stop the mixing, and then begin monitoring the progress before everything is already over. This situation also makes it difficult to attach a well defined “time zero” for the reaction since the mixing

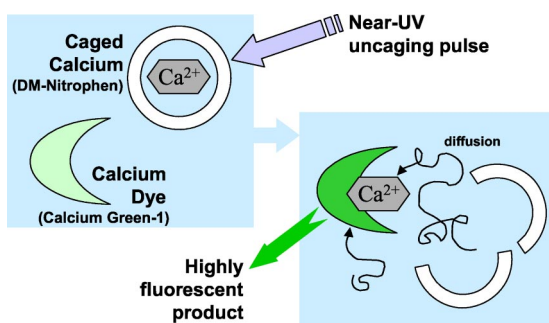


FIG. 1. (Color online) Schematic cartoon of the experimental chemical scheme used for monitoring the kinetics and initial condition memory for the $A + B \rightarrow C$ system.

itself takes time. A natural alternative would be to find a reaction in which some controlled, fast perturbation can dissociate a product into its component reactants. In this way it would be possible to have a well defined initiation time after which the reaction progress could be monitored. This effect has been observed and studied extensively [14], but it is a very specific initial condition called “geminate recombination,” in which the dissociation process induces a correlation between reactant pairs which strongly affects the outcome. The initial separation in the geminate case is usually so small, in fact, that this type of reaction is used to study the reaction half of the reaction-diffusion process, as diffusion becomes a negligible effect.

To circumvent these difficulties, we have used a scheme in which only one reactant is released by the perturbation, thus allowing a well defined start time without creating pair correlations. Specifically, as seen in Fig. 1, our A particles are calcium sensitive fluorophores, while the B particles are calcium ions which are initially bound to a cage molecule. On illumination by a pulse of near-UV light, the cage is photolyzed and the calcium becomes free to diffuse with the dye in solution until complexation occurs. Upon binding of a calcium ion, the dye’s efficiency of fluorescence increases dramatically, allowing monitoring of the reaction progress through high signal-to-noise visible wavelength fluorescence detection of product formation. With this system, then, the A particles have a random initial distribution, while the B particle distribution is defined and controlled by the UV pulse sample illumination.

Figure 2 explains in more detail the chemical processes at

each stage of the sample preparation and experimental reaction. An understanding of these steps is helpful both in interpretation of later results, as well as in appreciation of experimental requirements for the work. Schematic stages (a)–(f) of the levels of dye, cage, and calcium are shown on the left, with a corresponding fluorescence intensity (mock-up) graph shown on the right. (a) Shows the three chemical levels once the stock dye and cage molecules are combined in buffer, plus contaminating levels of calcium. In (b), extra calcium is added for the experiment. The stronger cage molecule binds most of the calcium ions, but its finite binding allows some calcium to bind to the dye initially. Then, in (c), the near-UV pulse photolyzes some percentage of the cage, both bound and unbound versions, allowing some of the calcium to be freed to diffuse and bind to the fluorescent dye in (d). (Note that in the (c) region of the graph the data “spikes” during the UV pulse.) This dye binding reaction leads to a maximum value for the dye fluorescence in (e), followed by a reequilibration of the system in (f), where calcium ions shift over to any unphotolyzed cage molecules (given their higher binding strength over the dye), causing the fluorescence levels to decrease a bit.

The first initial condition case described here is created by illuminating the sample chamber with “speckled” laser light delivered by an optical fiber. The second case is created by a flash lamp (noncoherent source) which delivers homogenous illumination over the sample.

Laser speckle is formed whenever highly coherent light interacts with a rough surface [15]. If this roughness is fairly random and microscopic, but on a scale long compared to the wavelength of the light, then the transmitted or reflected light is randomly shifted in phase on a very small spatial scale. This propagating light then interferes with itself, forming the well studied phenomena of laser speckle. While first seen as just an interesting annoyance to experimentalists, laser speckle is now being used in many fields. For example, over the past three decades, the techniques of speckle metrology have been developed to the point that the statistics of laser speckle are an important tool in the measurement of object shape, deformation, and material strain [16]. In our application, this patterned and statistically well defined light is used to set the spatial distribution of one reactant type, which is shown to strongly affect the resultant reaction progress. Three different stages are seen to occur in the reaction,

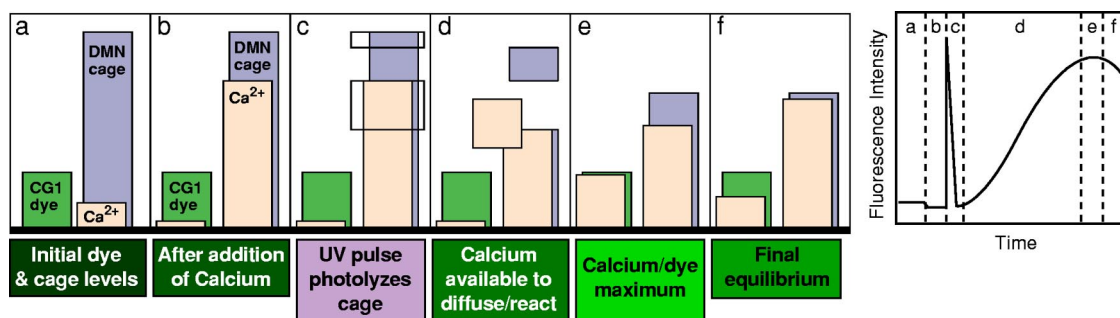


FIG. 2. (Color online) Chemical elements and levels during an $A + B \rightarrow C$ kinetics experiment. Stages (a)–(f) depicted schematically on the left are graphed on the right in preparation for later data presentation.

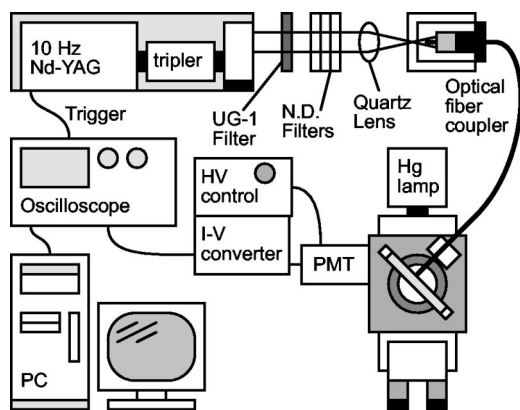


FIG. 3. Experimental equipment setup. UV pulses (1064 nm light tripled to 354 nm) are delivered to the sample capillary atop the microscope stage using a fused silica multimode optical fiber. Fluorescence excited by the mercury lamp (PMT detection) is recorded using a digital oscilloscope and downloaded to a PC for analysis.

which can be traced to the interesting spatial structure inherent in the speckled illumination.

In the following sections we will present the results of the two different reaction initial conditions, contrasting them with each other and with the classical case, showing a striking dependence of the reaction progress on the initial reactant distribution. Many of the ingredients for these experiments are familiar, but eventual success depended so strongly on detailed considerations for the equipment setup and chemical system that perhaps more space will be devoted to the *Methods* section than is standard, but it is believed to be necessary.

II. METHODS

The model $A + B \rightarrow 0$ (or C) experimental system consists of a calcium sensitive fluorophore combining with a calcium ion to produce a more highly fluorescent form of the dye molecule. Samples are produced by combining, in buffered aqueous solution, the dye, calcium ions, and a calcium cage molecule, which upon photolysis with near-UV light, releases its bound ion into solution making it available for binding with the dye (see Figs. 1 and 2). Neither the dye nor the cage is complexed with calcium ions as supplied by the manufacturers. The rise in fluorescence from the dye, monitored in the visible range, vs time, is then an indication of product formation, and thus, reaction progress.

A. Experimental equipment

Figure 3 shows a schematic overview of the experimental equipment setup. A pulse of UV light is generated by frequency tripling a ~ 10 ns pulse of 1064 nm light from a Nd:YAG laser to 354 nm. This beam then passes through a Schott UG-1 filter to further isolate the UV component, followed by optional neutral density filters for more fine power control. Optical fiber transmission of this UV pulse is used not only for flexible and compact delivery of the light to the sample, but also to clean up the beam profile and to generate

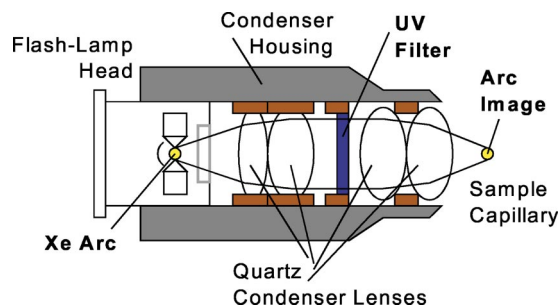


FIG. 4. (Color online) Flash-lamp condenser optics for efficient delivery of nonspeckled, near-UV light to the capillary sample chambers.

the speckle pattern for the “*B* landing.” The fiber coupling is accomplished with a 2 in. focal length G1 quartz lens (Esco Products), set to focus the light a millimeter or two before the end of the fiber. Adjustments are made so that the spot size matches the fiber face diameter, thus assuring a balance between maximal light coupling and minimal fiber damage from the UV light pulse. Fused silica fiber (Polymicro Technologies) with a $500 \mu\text{m}$ core diameter then runs to the sample stage atop an Olympus IX70 inverted optical fluorescence microscope [18]. A mechanical XYZ translator bolted to the stage is used to position the fiber at the sample chamber, while microscope stage XY translation can be used for sample alignment with the detector. Fluorescence monitoring is carried out using a 100 W mercury arc lamp and filters (Olympus narrow blue cube) in an epi-illumination geometry. The fluorescence signal is delivered to a photomultiplier tube (PMT) at the side port of the microscope, with variable high voltage (HV) supplied by a Bertan model 205A-03R. After current to voltage conversion (transimpedance amplifier), the signal is digitized and stored by a Tektronix TDS 420 oscilloscope—data acquisition being triggered either by a *Q*-switch output pulse from the laser, or by the voltage trigger signal for the flash lamp. Either Tektronix TEKDIG software, or custom coded software is then used for GPIB acquisition to a PC (DFI Pentium 166) for processing and analysis.

For nonspeckled irradiation of the sample chambers for uncaging, a Hamamatsu model L7684 60 W xenon flash lamp was used with optional external $4 \mu\text{F}$ capacitor and model C6096 1000 V power supply. This unit is capable of generating 2 J/flash over the whole xenon spectrum, but requires a very efficient condenser to deliver enough near-UV light to uncage proper amounts of calcium in the sample chamber for the kinetics experiments. The effective *f* number of this condenser and the amount of aberration induced by the available, short focal-length quartz lenses are the main limiting factors in the flash-lamp initiated reactant production. Figure 4 shows a schematic diagram of the flash-lamp condenser built for this application.

Samples are held in various sizes of quartz and fused silica capillaries. This confinement not only avoids fluid convection, but also keeps the sample solution from moving when hit with the UV pulse. The sample materials are chosen to minimize fluorescence and phosphorescence under the UV illumination. Fused silica capillaries of $10\text{--}100 \mu\text{m}$ I.D.

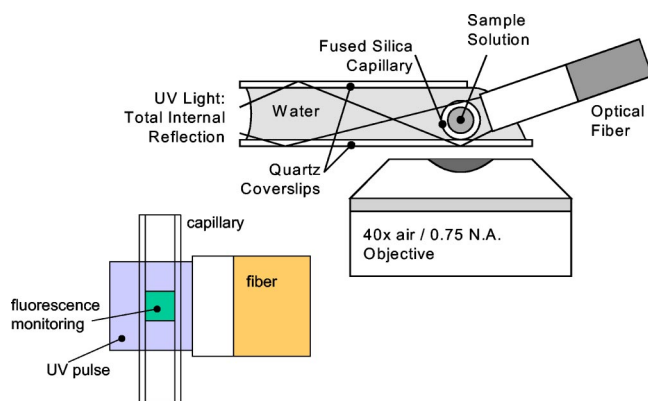


FIG. 5. (Color online) Small capillary sample chamber (side on, upper right) with optical fiber UV pulse delivery. Total internal reflection (TIR) and close index matching reduce stray light into the microscope objective and later detection system. Lower left: A larger area is always flashed with the near-UV pulse than is used for monitoring the fluorescence of reaction product production.

were obtained from Polymicro Technologies, with a polyimide protective coating. This coating was removed in fuming sulfuric acid, and the tubes were mounted with heat glue in the ends of syringe needles to facilitate sample loading and capillary rinsing. A separate microscope (from the one used for data acquisition) with $43\times$ objective, stainless steel capillary guides, and a syringe holder, was used to observe and verify sample loading.

We found that even with quartz and fused silica sample holders a significant pulse remained at the beginning of each data set, probably due to phosphorescence and fluorescence from the fiber, as well as UV light which is not filtered completely before the detector. Delivery of the UV pulse at 90° to the detection optics helped minimize this “data spike” artifact signal, but when small diameter capillaries were used for the sample chamber, a considerable amount of light was reflected off the lower portion of the capillary, down into the microscope optics and detector. So, for small diameter chambers, we implemented a sample holder which uses total internal reflection (TIR) and closer index matching to steer the unwanted light away from detection. Figure 5 shows a side-on schematic of this sample geometry. One millimeter quartz spacers (not shown, but parallel to page plane) were placed a few millimeters apart and sandwiched between two quartz coverslips (Esco Products—the top coverslip having been cut down in size), creating a small rectangular tube on top of the larger coverslip, open on both ends. Along one end was placed the $50\ \mu\text{m}$ I.D. capillary sample chamber (sticking out of the page plane in the diagram) with the UV delivery fiber brought in at a shallow angle from the other side of the capillary. As long as this angle, plus the half angle of the exit light from the fiber (taking into account that the fiber end is submerged in $n = 1.33$ water) is less than the cutoff angle for TIR at the quartz/air interface, most of the impinging light will be not only directed past the objective lens, but also past the rest of the face of the objective (to avoid burning the surface with the UV pulses). The rest of the advantage was achieved because of the closer index match of water to the capillary fused silica (over air), resulted in less reflec-

tions down into the detection system [19].

For flash-lamp initiated uncaging, direct illumination of the sample chambers was utilized because more light could be delivered with this method (due to insufficient coupling of Xe lamp light into the optical fiber). The move from fiber delivery to direct, focused light forced us to abandon the TIR sample holder in the flash lamp runs due to more extreme angles of incidence with the focused light, as well as issues with the beam traveling through the air-water interface. Also, $75\ \mu\text{m}$ I.D. capillaries were used for the sample chambers in the homogeneous illumination (flash-lamp) experiments, where the spot of near-UV light delivered to the sample was larger than in the laser case.

With the precautions detailed above, the initial spike in the detected kinetics data was still problematic when using the flash-lamp initiation (due to the longer pulse— $10\ \mu\text{s}$ vs $10\ \text{ns}$). This limited the useable flash-lamp data to readings starting after about $10\ \mu\text{s}$.

The UV illumination pattern at the end of the delivery fiber was imaged in two different ways. First, as a rough check of pattern consistency between pulses, a piece of smooth, white thermal paper was placed a few millimeters from the end of the fiber. Each laser pulse produced a burnt spot on the paper, within which patterns could not be distinguished with the naked eye, but under magnification each spot could be compared to check the consistency of the illumination pattern from pulse to pulse. At least 95% of the spots produced were consistent between each firing pattern recorded. Imaging with a more linear response device was performed with a Princeton Instruments charge-coupled device (CCD) camera, by placing an American Optical $43\times$, N.A. 0.66 microscope objective between the fiber end and the camera. Single pulses could then be recorded and stored on disk for analysis.

B. Data acquisition

The procedure for data collection included a preliminary check of rough uncaging behavior, including a coarse adjustment of UV pulse energy, followed by the acquisition of more detailed kinetic data. Pulse energies varied between $20\ \mu\text{J}/\text{pulse}$ and $1000\ \mu\text{J}/\text{pulse}$, with the most used range at the lower end, centering on about $100\ \mu\text{J}/\text{pulse}$. Flash-lamp pulse energies were about half the laser values, and the focused spot was about twice as large, causing the energy density for uncaging to be about one-fourth the laser-pulse levels. In all experiments, the capillary region exposed to the UV pulse was about twice as long as the segment monitored for the kinetics (fluorescence—see Fig. 5, lower left), so that any components diffusing in and out of the monitored region had been exposed to the UV uncaging pulse. With the internal oscillator of the Nd:YAG laser set at 5 Hz, an initial check of the uncaging behavior was made. (The number of pulses required to saturate the dye fluorescence is an indication of the percentage of cage photolyzed with each pulse—see Fig. 6 for an example of this behavior.) This procedure also allowed the PMT high-voltage supply to be set so the initial and final signals fell within the vertical oscilloscope range ($0\text{--}800\ \text{mV}$ used consistently). Although this prelimi-

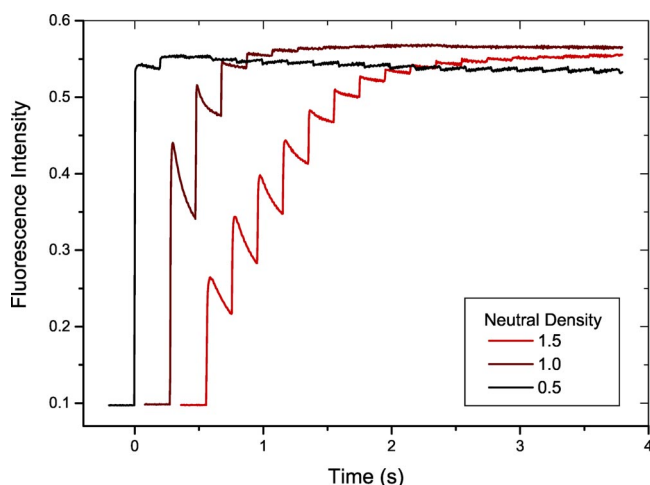


FIG. 6. (Color online) Typical multipulse uncaging behavior of DM-Nitrophen™ as monitored with Calcium Green-1™ (CG1). Curves are offset in time for ease in viewing. As UV intensity is increased (less neutral density—curves to the left), fewer pulses are required to saturate the dye response, but photobleaching with each pulse is also increased. The two lowest power traces also show a signal decrease between pulses, characteristic of the fact that competitive binding of calcium ions between the dye and any unphoto-lyzed cage molecules favors the cage (see Fig. 2).

nary data was not always used for later analysis, it was saved to allow comparisons between different sample preparations. It also revealed the various effects of photobleaching which are mentioned in more detail below. Once rough settings were fixed, and qualitative behavior of the chemicals was verified, the time scale was changed to 200 $\mu\text{s}/\text{division}$ and the laser switched to single-shot, remote control mode, where a single laser pulse initiated the reaction and triggered data acquisition. Between each data set, the capillary was moved a few millimeters through its guides to a previously unilluminated segment of the sample chamber.

The kinetic situation most studied in theory and simulations is that of equal initial A and B populations. Therefore, in principle, it would be preferable to identify and reach the fine balance of UV intensity required for exact calcium uncaging matching the solution dye concentration for each experiment. A more practical approach was necessary in practice. The initial coarse adjustment was made to the near-UV pulse energy as described above, then a range spanning the approximately equal population uncaging point was used during each experiment. For the laser initiated reactions, intensities were adjusted with neutral density (ND) filters, spanning about ND one, in increments of 0.1–0.3. For the flash-lamp experiments, pulse energy was adjusted using the variable high-voltage supply in 250 V increments to the 1000 V maximum.

C. Chemical environment

The ideal chemical components for studying an experimental $A+B\rightarrow C$ system would be one in which both cage and sensor molecules have infinite binding strength, and the sensor would have very bright fluorescence when unbound and none when bound to the ion. (Plus, the ion and fluoro-

phore would have identical diffusion coefficients, although this tends not to be that important [20].) Calcium ion cages and fluorescent reporters were chosen in this case because they fit closely with this ideal model. In reality, though, the best calcium sensors are characterized by an increase in fluorescence upon calcium binding, rather than a decrease, so the real experiment follows product concentrations instead of the more ideal (for theoretical reference) reactant concentrations. Also, all of the bindings are somewhat reversible, so we work with initial and final equilibria rather than the clean, irreversible, theoretical case. DM-Nitrophen™ was chosen for its characteristic combination of stronger binding than the calcium dyes, and a good product of extinction coefficient and quantum efficiency for uncaging [21–25]. Nitrophenyl EGTA (NP-EGTA) was also tried, but its weaker binding make it less useful for this application, and the controlled conditions in this experiment do not require NP-EGTA's increased specificity for calcium over magnesium, which favors it for biological applications [22,26–28]. Calcium Green-1™ (CG1), from Molecular Probes, was chosen as the reporter for most experiments. It has bright fluorescence, reasonably strong calcium binding, visible light excitation (so that the fluorescence monitoring doesn't uncage calcium by itself), and a good ratio of calcium bound to unbound dye fluorescence intensity [29,30]. (A ratiometric dye would be more ideal, in principle, so that effects such as photobleaching would not affect the results.) Fluo-3 is another calcium sensitive fluorophore with visible excitation and other similar properties to CG1, which should make a fine alternative. Calcium Green-2™ was used for some initial tests because of its larger fluorescence increase upon calcium binding, but its weaker binding wasn't as ideal here. Calcium Orange™ also worked fine, but has a smaller fluorescence change with binding.

The choice of chemical environment was tailored to kinetics work rather than the more standard physiological conditions used for chemical sensing and intracellular studies. Almost all published values for binding and kinetic constants, and any preprepared calibration buffers, are for conditions around neutral pH with an ionic strength around 100 mM [22,23,29–37]. The parent compounds of these chemicals, though, BAPTA [38] for CG1, and EGTA and EDTA for the calcium cages [39], exhibit drastic changes in their binding properties with solution environment [35,40,41]. Independent tailoring of these binding strengths is possible to some extent since calcium ion binding to BAPTA has little pH dependence above pH 7, while EGTA still has a strong increase in calcium binding through the basic range. Ionic strength of the buffers, on the other hand, affects BAPTA binding more strongly than EGTA. For this application, then, it was necessary to raise pH and lower ionic strength to decrease the dissociation constants of both compounds. In order to test and model the multiple equilibria, we used the freeware PC buffer calculation program *WinMaxC.exe*, and its associated Windows tool *Sliders.exe*. These programs also allow us to calculate how many pulses it will take to saturate the dye response during experiments (as shown in Fig. 6) when the UV pulse uncages enough calcium to equal the amount of unbound dye present in the initial equilibrium.

The nonclassical kinetics theoretical literature shows that the asymptotic effects which are so interesting, emerge at

various times depending on the initial reactant density, but that there is a consistent ratio of reactant density at crossover to initial reactant density when these effects begin to appear [42]. Therefore, solution conditions for experiments are only useful if the resultant binding strengths are high enough that the initial and final reactant densities go well through the necessary ranges predicted to be required in the literature. As noted before, tighter binding, and thus a greater range of densities through which the reaction will proceed, can be achieved by raising pH and lowering ionic strength. On the other hand, straying too far afield from physiological conditions, under which the body of literature on these chemical characteristics was published, could lead to unexpected behaviors of the chemical elements, e.g., their interactions with each other and with the sample chambers in these restricted environments.

A Tris-HCl buffer [Fluka Tris(hydroxymethyl)aminomethane plus HCl], with pH 8.5 and ionic strength of 11 mM (2 mM KCl) was chosen to achieve this balance, and titrations were conducted to confirm the general effects of changing ionic strength and pH. Quantitative calibration of the dye and cage binding is difficult, though, under these strong binding conditions since electrodes used to calibrate the buffers are not accurate below pK_{Ca} of about seven [43]. Finally, titrations were done under experimental buffer conditions to set the initial amount of calcium to add to the combination of calcium dye and cage for the kinetics studies. This allowed compensation for slight variations in the concentration of each reactant as supplied and diluted, and adjustment for any impurity calcium (since the purity of some compounds are not known and have been observed to vary from batch to batch). After balancing the equilibria requirements and considering how much cage would need to be photolyzed vs photobleaching of the dye, reagents were used at about 48 μM cage, 36 μM Ca^{2+} , and 10 μM CG1 in 200 μl sample volumes. Samples were prepared by pipetting dye into the buffer, after which calcium chloride is added. The dye/buffer solution should not be very fluorescent by itself (the eye and a flashlight are sufficient for this rough check), and a dramatic color change and rise in fluorescence should be seen upon the addition of calcium. Finally, the cage is added to the solution, at which point the sample color should shift back to its original (precalcium addition) state.

The flash-lamp source for near-UV pulses has lower energy density than the laser (speckled source), which necessitated different chemical conditions for equal initial reactant densities. As can be inferred from Fig. 2, if there is not enough light to uncage sufficient calcium, the other way to release more calcium with each pulse is to have more cage and calcium present initially. At the same binding strength, though, the result would be to fill more of the CG1. As a result, a further modification to the chemical environment was necessary for the homogenous, flash-lamp initiation. This comprised a higher pH (10.1), carbonate buffer, which increased the binding strength of the cage without affecting the dye binding significantly. Under these conditions 54 μM calcium and about 60 μM DM-NitrophenTM could be used along with the same 10 μM CG1 in 200 μl sample volumes. Because the balance of initial unbound calcium level was

more critical in these experiments, titrations were done on each sample preparation while monitoring fluorescence levels from the CG1 such that the added cage dropped the fluorescence down to just under 10% of the maximum (calcium saturated) level.

The “data spike” artifact mentioned above (see illumination methods description) force flash-lamp experiments to be conducted in a higher viscosity, 50% glycerol environment to slow down the kinetics. This additionally complicated the small volume sample preparations such that an apparatus had to be created which could vortex the sample while simultaneously allowing CG1 fluorescence readings for the titration.

Another consideration which must be made when using small diameter capillaries as sample chambers is the presence of silica surface charges. As the tube diameter is reduced, the ratio of edge surface to sample volume increases, and attention must be paid to possible consequences of this static charge such as effective pH change [44]. The interface between the glass and aqueous phases sets up an electrical double layer of negative surface charges and positive ions in the solution. The Debye-Hückel parameter, used extensively in electrophoresis and colloid sciences, gives us a measure of the thickness of this layer, or more precisely, the $1/e$ point of an approximately exponential decay of the potential, depending mainly on the solution electrolyte concentration [45]. In aqueous solution at 25 °C, this relationship can be reduced to $\kappa = 3.288\sqrt{I} \text{ nm}^{-1}$ where I is the ionic strength of the solution, and $1/\kappa$ gives us the double layer thickness in nanometers. At 10 mM ionic strength (characteristic of our experimental environment as described above) the surface charges should be shielded to about 2% by $(3/\kappa) \sim 10 \text{ nm}$. Thus, we would not expect these surface charges to have a large effect on our results since this depth is about 0.01% of the capillary diameter in most cases.

Other properties of the chemical system had to be taken into account, and/or compensated for, within this series of experiments. Although CG1 is a visible excitation fluorescent dye, this whole family of dyes has significant absorbance in the near UV as well. So, photobleaching of the dye with the UV uncaging pulse became an issue, besides any photobleaching due to the continuous visible excitation light from the mercury lamp. Efforts can be made to compensate for this photobleaching in the analysis stage, although the variety of UV pulse energies used, as well as the differences in bleaching efficiencies for bound and unbound dye molecules make this difficult. But, it was found that in addition to these expected effects, there was some sort of “reversible photobleaching” with each pulse [46,47], happening on a similar time scale to the reaction progress itself. Avoidance of this effect is sometimes possible with the same remedies used for the photobleaching itself. The histology literature is filled with studies of various antifade agents used to counteract dye photobleaching [48–51]. Many of these were evaluated for our specific application, including iodide ions, 1,4-diazobicyclo(2,2,2)octane (DABCO), glycerol, *n*-propyl gallate (NPG), and *p*-phenylene diamine (PPD). Although much work has been done in various labs to find a suitable substitute for PPD since it is a skin sensitizer, we found the same thing as many others have that it was the best choice

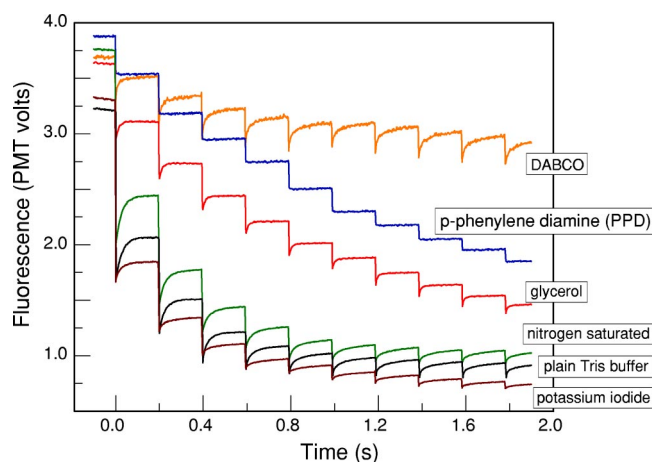


FIG. 7. (Color online) Typical multipulse, reversible photobleaching results showing the effect of various antifade agents on Calcium Green-2TM in Tris-HCl buffer. Initial (negative time) fluorescence levels are somewhat normalized using the PMT variable high voltage supply. Agents modify the steady-state photobleaching (Hg lamp), the UV pulsed photobleaching, as well as the reversible photobleaching; *P*-phenylene diamine is the only effective additive for elimination of the reversible behavior.

available for this application. PPD was dissolved at 1 mg/ml in the buffer solution, or at 2 mg/ml if using 50% glycerol along with the buffer. (This increase in PPD levels for the glycerol case was found to be necessary to reach the same beneficial effects as in plain buffer. This agrees with the idea that PPD might act through some sort of diffusion-mediated collision with the excited dye.) Care must be taken since PPD is a skin sensitizing agent, and oxidizes rapidly in light and heat, turning dark brown.

Studies of the dye alone in buffer under the UV pulse illumination revealed a 50–100 μ s rise in fluorescence of the dye after each UV laser pulse accompanying the photobleaching. Figure 7 shows some characteristic results in various solution conditions with buffer additives commonly used for the reduction of photobleaching. Results are roughly normalized by PMT high-voltage adjustment since almost all antifade agents change the steady-state fluorescence level. It is clear from this plot that the PPD was the most effective in eliminating the reversible photobleaching and works well in reducing the pulsed photobleaching, while it also minimizes the steady-state destruction which occurs under the constant mercury lamp monitor illumination (data not shown). It is not clear why PPD was the only compound which proved effective against the reversible photobleaching, or what mechanisms are involved.

D. Data logarithmic smoothing

Voltage (intensity) data recorded by the oscilloscope necessarily has a linear spacing in time. In contrast, many of the anomalous kinetic behaviors of the $A + B \rightarrow 0$ system scale in time in an algebraic manner. This discrepancy between acquisition and analysis scales leads to unnecessary detail at long times, while loss of detail on short-time scales could be ruinous. Therefore, we implemented the same data smooth-

ing routine as in Lin [52] which averages intensity readings over a larger and larger window as time progresses. The algebraic increase in bin size results in evenly spaced data points on a logarithmic time axis—retaining the detail at short times while averaging over extraneous detail at long times. This method does not “throw out” any data, but still reduces considerably the number of data points to view and increases the statistical significance of later points. The original linearly spaced data points are always retained in case changes in analysis are later required.

E. Fluorescence Relationships

Reaction progress is followed experimentally by monitoring the increase in fluorescence of the calcium sensitive dye. This signal, though, may not be the desired quantity in two respects: It includes a fluorescence contribution from both the unbound dye and any background signal present, and the main portion of the signal reflects product production rather than the more commonly referred to quantity of reactant density. We can explicitly state the definitions we have worked with so far in relating the experimental system to the model $A + B \rightarrow C$ reaction:

$A \equiv [\text{dye}]_f$, the concentration of unbound (f denotes free) dye in the solution,

$B \equiv [\text{Ca}^{2+}]_f$, the concentration of unbound calcium ions, and

$C \equiv [\text{dye}]:[\text{Ca}^{2+}]$, the amount of the dye with calcium complex present.

Additionally, we define D as $[\text{dye}]_{\text{total}}$, and b is the *background fluorescence intensity*. The fluorescence of the bound and unbound forms of the dye each have an associated quantum efficiency, which will depend on the specific experimental conditions. We can denote these quantities as multiplicative constants, such that α is the *bound* dye fluorescence efficiency and β denotes *unbound* dye fluorescence efficiency, then the maximum possible fluorescence signal is

$$F_{\text{max}} = \alpha D + b = \alpha[A(t) + C(t)] + b$$

(*independent of time*) and the signal measured in time is

$$F(t) = \alpha C(t) + \beta A(t) + b.$$

So, with these relations, a quantity proportional to the reactant density can be calculated from the experimentally measured fluorescence with the relation

$$\begin{aligned} F_{\text{max}} - F(t) &= \alpha[A(t) + C(t)] + b - [\alpha C(t) + \beta A(t) + b] \\ &= (\alpha - \beta)A(t). \end{aligned}$$

And, similarly, the initial A concentration A_0 can be obtained from the quantity $(F_{\text{max}} - F_0)$.

It is important to note that while these quantities are important for comparisons with theoretical results, the measurement of F_{max} is problematic in many ways, and introduces significant error. This error becomes troublesome in some of the time regions of interest since we are often looking for

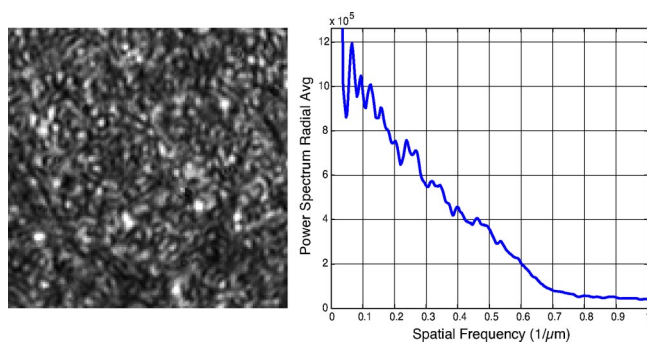


FIG. 8. (Color online) *Left*: Experimental image showing the UV intensity distribution on a section of the delivery fiber face (image shows a $65 \times 65 \mu\text{m}$ region). This type of pattern is characteristic of laser speckle. *Right*: Radial average of the speckle image two-dimensional Fourier power spectrum. The triangular shape is expected for imaged laser speckle, and shows an $\sim 1.4 \mu\text{m}$ speckle size. (The DC peak extends above the presented y axis.)

asymptotic behaviors where F and F_{max} will not necessarily differ considerably. Variations in optical alignment of the sample, in local concentrations within the capillaries, and in sample state over time in the sample chamber make it necessary to measure F_{max} in the same spot that the reading of $F(t)$ is taken. But, photobleaching by the uncaging light and diffusion of all components from outside the illuminated and monitored regions make it difficult to take an accurate reading of this quantity. Because of this, comparisons are often made to simulation results in the form of product (C) production vs time, rather than in the more standard reactant (A) density, or reaction progress ($1/\rho_A - 1/\rho_{A0}$).

III. RESULTS

Typical uncaging behavior can be seen with a multipulse measurement, as was seen above in Fig. 6. All of these curves have features in common which help evaluate the effects and effectiveness of the uncaging process. Acquisition is triggered with the first UV pulse, so negative time represents the resting fluorescence level—a combination of background, unbound dye fluorescence, and prepulse equilibrium, bound-dye fluorescence. The laser clock rate is set at 5 Hz to give adequate relaxation time for behavior viewing. Early pulses give a rise in fluorescence as calcium is uncaged. At the lower powers this rise is followed by a drop in fluorescence due to calcium leaving the dye and rebinding with unphotolyzed cage molecules (as explained in Fig. 2). (Stronger binding of calcium to the cage over the dye hinders long-time measurements in this way, but it must be remembered that this is also what allows the experiments to be carried out at all, since we require most of the calcium to be initially bound to cage rather than dye.) Eventually, enough pulses have been delivered that the amount of uncaged calcium is sufficient to saturate the dye binding, and no more intensity increases are seen with each pulse. After this saturation point, at all but the lowest powers, the effects of UV pulse photobleaching can be seen as time goes on.

Figure 8 (left) shows a typical image of the speckles used to initiate the spatially correlated reactions. The radial aver-

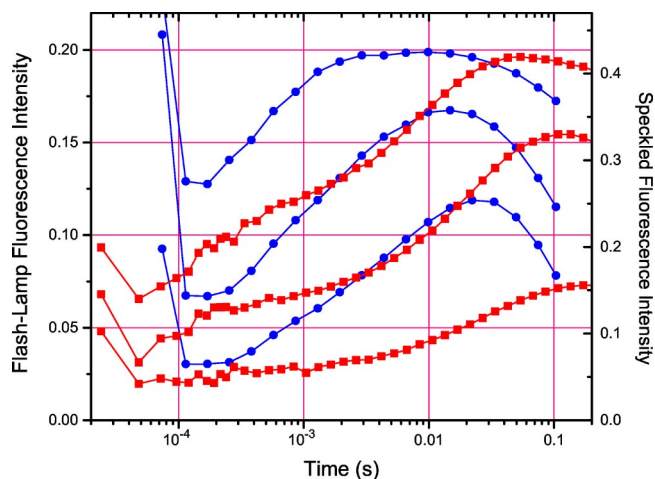


FIG. 9. (Color online) Product fluorescence vs time at various UV uncaging powers for CG1, DM-Nitrophenol™, and Ca^{2+} . Circles indicate flash-lamp initiated reactions and square symbols indicate laser-initiated (speckled) results; UV pulse artifacts mask the fact that all flash-lamp curves begin at about 0.05 V and all laser curves start at around 0.02 V. Flash-lamp results show a monotonic rise in product with time, while the speckled results show a fast initial rise, followed by a very slow interval of product formation, then a subsequent increase in rate.

age of a two-dimensional Fourier power spectrum (using Matlab) shows the general triangular shape characteristic of imaged speckle patterns [15,53] as shown in Fig. 8 (right). The high spatial frequency tail of the spectrum falls off to zero at a value corresponding to about $1.4 \mu\text{m}$ on the fiber surface. This value represents the average speckle size, and has about the expected order of magnitude since the speckled light hasn't propagated far enough in free space to allow much expansion of the apparent speckle size. It is a bit difficult in this case to go any further with expectations about the speckle characteristics since they are actually formed in a nontrivial way when the inhomogeneous beam profile is focused into and travels through the 2 m of multimode fiber. The overall spatial distribution seems quite similar, though, to the simple models of laser speckle generation [19].

Figure 9 shows two typical series of fluorescence (related to reaction product concentration) vs time measurements with three UV pulse powers (each) used for uncaging. The logarithmic x axis helps in viewing the changing behavior over many decades of time. Circular symbols are for data from flash-lamp initiated experiments, while squares are for speckled, laser initiated runs. (Flash-lamp results have been shifted (to the left by division) in time by a factor of $6 \times$ to compensate for the fact that these experiments were performed in 50% glycerol, and to allow more direct comparison with speckled results in standard viscosity aqueous buffer.) Each set of data includes three curves, each at a different UV pulse energy. The middle curve of each set is the approximately equal initial A and B concentration situation (as judged by the multipulse uncaging experiments described in the *Methods* section). At early times, the data shows the artifact from the near-UV pulse, ending at about $20 \mu\text{s}$ for the laser results and at about $100 \mu\text{s}$ for the flash-

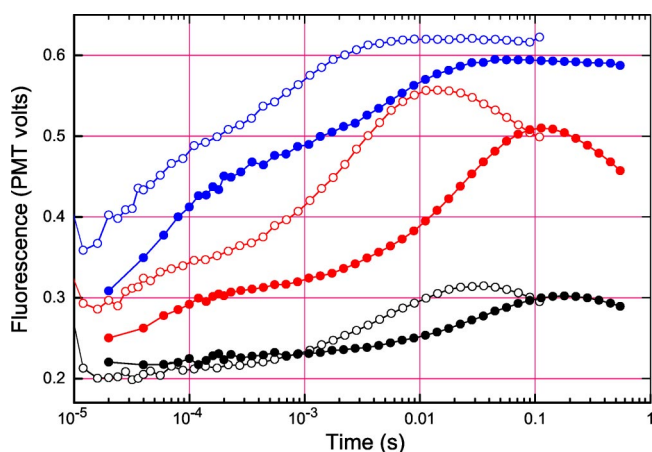


FIG. 10. (Color online) Comparison of calcium-dye complexation reaction in 50% wt:wt buffer-glycerol solution (open symbols) along with reaction results in buffer without glycerol (closed symbols). UV pulse energy varies by about a factor of three (ND 0.5) between curves in each set. A delay in the reaction features can be seen, proportional to the calculated viscosity ratio of 6, showing the effects and importance of diffusion in the kinetic features.

lamp experiments, masking the fact that the speckled curves (squares) all start at about 0.02 V and the flash-lamp curves all begin at about 0.05 V. All of the curves then rise in some way as product is formed over time. A decrease in all the curves can be seen at later times due to the fact that calcium binding to any unbound, unphotolyzed cage molecules is favored over binding to the dye. (See *Introduction*, Fig. 2 stage (f), and *Results* description of Fig. 6.)

The flash-lamp curves all show a simple structure, with a monotonic rise in product over time. As would be expected, higher UV pulse energies lead to faster product formation, due to the correspondingly higher initial B concentrations. (Higher product formation rates are indicated by steeper slopes of the product density vs time curves.)

The product formation fluorescence in the speckled case is not as straightforward, showing a variety of structure (most clearly seen in the middle curve, but present in all three) *with an early fast rate of product formation, followed by a slowing of the product formation rate, then by another rise in that rate.* (Again, we will refer to the change in reactant or product density in time as an indicator of the overall reaction rate.)

In an effort to explore the robustness of the kinetic features observed, Fig. 10 shows the effects of running the laser-initiated experiments in a 50% wt:wt glycerol:buffer solution along with a comparison to the plain buffer solution reactions. The fluorescence levels have been normalized using the high-voltage control on the PMT detector, since the fluorescence response range, bound to unbound, of the dye decreases by about 30% in this higher viscosity medium with $2 \times$ PPD (for reversible photobleaching removal—see *Methods* section). UV pulse powers were varied by about a factor of 3 (N.D. 0.5) between curves for each set. Here we see practically identical behaviors under the two conditions, with one set delayed in time by a factor close to the calculated

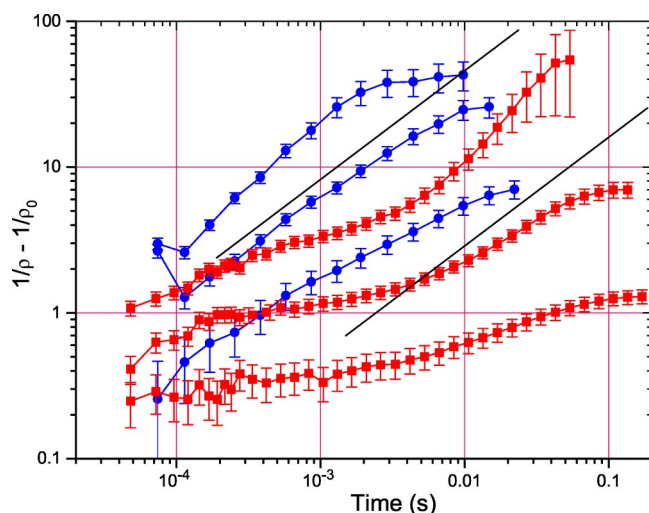


FIG. 11. (Color online) Reaction progress vs time calculated from experimental data shown in Fig. 9 taken at three different UV pulse energies (low to high going from bottom to top). Again, circular symbols indicate flash-lamp initiated reactions (homogeneous illumination) and square symbols denote laser-initiated reactions (speckled). The straight lines have a power law slope of 0.75, which is equal to the three-dimensional Zeldovich asymptotic rate for the $A + B \rightarrow 0$, equal density annihilation reaction.

viscosity ratio of 6. This verifies the contribution of the diffusion limitation to the reaction rate regimes.

IV. DISCUSSION

The results obtained show reaction rates which differ significantly over time, for the same elementary, binary, $A + B \rightarrow C$ reaction, but under quite different initial reactant distributions. The A reactant was always randomly distributed through premixing of chemicals, but the B reactant was distributed according to the intensity distribution through the sample chamber of a near-UV pulse of light. When reactions were initiated by a pulse from an incoherent light source, forcing an apparently initially random B distribution, the product formation over time looked qualitatively similar to the classical case, with monotonically increasing product until the limitations of the experimental chemical system were reached. The laser-initiated reactions, on the other hand, gave the B distribution an apparently speckled initial distribution, and the reaction product formation went through three identifiable regimes, with an initially fast period of product formation, followed by an extremely slow region, then followed by another fast regime. We will look at these results quantitatively with rates of reaction progress, as well as comparisons to Monte Carlo simulations to test whether speckles are indeed sufficient to cause these anomalous reaction rate regimes.

If we return to the experimental fluorescence intensity vs time information, including now the measurements of the maximum fluorescence intensity for a given set of data, we get plots such as in Fig. 11. This is a plot of experimental reaction progress vs time on a \log_{10} - \log_{10} scale using the same data as in Fig. 9 (again, circles are flash-lamp initiated

reactions and squares are speckled, laser initiated). As described in Methods section, the fluorescence intensity is subtracted from the maximum possible intensity for that experiment in order to obtain values proportional to the reactant density. Then, the reaction progress is calculated by subtracting the inverse of the calculated initial density from the inverse of this time-dependent reactant density. The error bars seen in the figure are dominated by the uncertainty in the determinations of F_{max} and F_{min} . The Zeldovich asymptotic behavior of the reaction progress ($1/\rho_A - 1/\rho_{A0}$) for the $A + B \rightarrow 0$ reaction goes as $t^{d/4}$, and the solid, straight lines in the plot indicate the three dimensional, power law slope of 0.75, for comparison to the data. Even though this result has not been seen before experimentally, it is not too surprising that the initially random case (flash lamp) has a slope near the asymptotic Zeldovich behavior. The speckled case, on the other hand, is additionally interesting in that after the slow, mid-time regime, the curve appears to also follow the Zeldovich rate for a while during the later time regime! This behavior is only observed over about one decade of time, though, so we need to understand more about the reaction occurring after this type of initial reactant distribution to see whether this result is important, or merely a coincidence. It is essential to recall, though, that in the “classical” case, none of these reactions would show these slow rates ($1/\rho$ should go as t^{-1}), and none of them should show any dependence on initial reactant *distribution*.

The excellent agreement between the experimental data and the Zeldovich rates during some part of the kinetics is encouraging, but this does not explain the very slow kinetic regime during the mid time of the laser-initiated reactions. In fact, this slow period is even less active ($(1/\rho) \sim t^{0.18}$) than the one-dimensional Zeldovich case for initially random reactants ($(1/\rho) \propto t^{0.25}$). Further, it is the existence of this exceedingly slow regime, delaying the onset of the randomlike behavior and in contrast to the flash-lamp initiated kinetics, which indicates most strongly that we are observing nonclassical kinetics.

In order to test whether a speckled initial B distribution was sufficient to lead to this sort of fast-slow-fast rate behavior, we conducted Monte Carlo simulations of an $A + B \rightarrow 0$ reaction (as described in Refs. [10,9], and in more detail in an upcoming publication). Since we observed that the laser light was speckled, but didn't have access to any details of the exact three-dimensional light distribution inside the capillary, a three-dimensional simulation was not easily feasible. Instead we used the simplest cases, with two-dimensional random and speckled B distributions, as a crude test to see if the spatial fluctuations present in the speckle pattern would be sufficient to produce the qualitative features we observed in the experiments. The Monte Carlo approach (as opposed to a solution of reaction-diffusion equations) is the most straightforward for imposing the speckled initial B distribution. Furthermore, since $d=4$ is the crossover dimension for $A + B \rightarrow 0$ into classical behavior [3,4], the three-dimensional Zeldovich slopes would be $d/4$ and the qualitative behaviors would be the same in one and two dimensions (2D) (both of which we simulated, but only show the two-dimensional results here). Therefore, performing the full three-dimensional

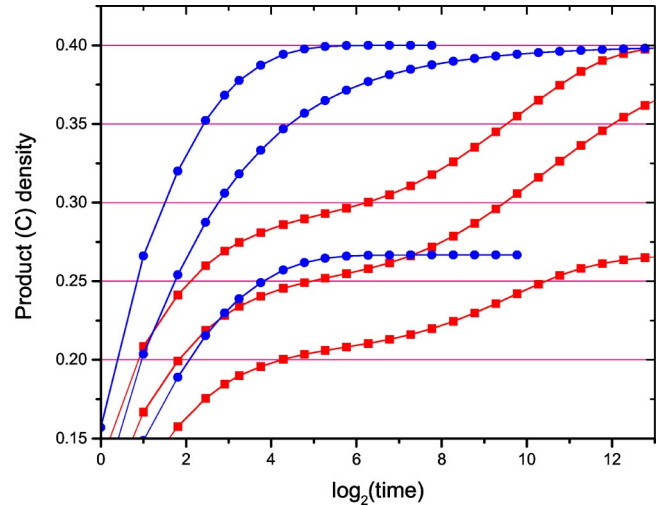


FIG. 12. (Color online) Simulated product formation for both initially random (circles) and initially speckled (squares) B conditions. For comparison to the experimental conditions, the initial A reactant density was held constant and the distribution was spatially random, while the B initial density was varied ($0.5\rho_{A0}$, $1.0\rho_{A0}$, and $1.5\rho_{A0}$).

simulation would not reveal any new insights into the roots of the kinetic regimes, while adding computational restrictions. Fig. 12 shows simulation results for both initially random B distributions (circles), as well as the contrasting initially speckled case (shown in square symbols). Already it is qualitatively obvious that these two cases give very different results, and that the speckled B reaction exhibits the characteristic fast-slow-fast product formation regimes as in the experiments. In these simulations, competition of the calcium for unbound cage molecules is not included (although simulations were conducted, but are not shown here for simplicity), but a difference between the random and speckled cases can also be seen from the time at which the reactions approach their apparent saturation point. Just as in the experiments, one must wait much longer for the speckled reactions to “end,” due to the delay from the intervening slow regime. One difference between the experimental and simulation results is an apparent discrepancy between the relative initial populations between the three runs of each set. This was not explored further, but it is obvious that while we have confidence that our experimental runs included the equal initial A and B density points, the higher and lower initial populations were not exactly proportional to either the optical density of the filters before the coupler in the laser case, or to the high-voltage supply setting in the flash-lamp experiments. Despite this, the agreement between simulation and experiment is remarkable.

In order to view the simulation data more quantitatively, Fig. 13 shows the reaction progress for the same Monte Carlo simulation results as shown in Fig. 12. Again, the circles are for initially random B distributions, and squares show initially speckled B reactions. Solid lines show the slope for the asymptotic Zeldovich rate behavior in 2D of $t^{1/2}$. As can be seen in the plot, the initially random, initially equal A and B density reaction asymptotically approaches the Zeldovich rate, and so does the initially speckled case. After

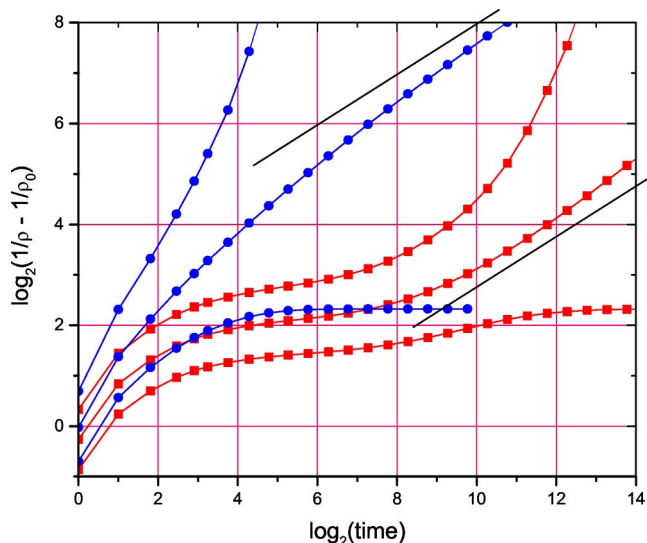


FIG. 13. (Color online) Simulated reaction progress for both initially random (circles) and initially speckled (squares) conditions.

the slow regime, the equal initial density curve follows the one-half slope line quite well.

It is beyond the scope of the present paper, but further spatial analysis of the simulation results has shown that the fast-slow-fast product formation rate behavior is a direct result of the spatial scales present in the laser speckle. The power spectrum in Fig. 8 shows that over a certain range of spatial scales, the speckled distribution has additional fluctuations present over the random case. The results are most easily understood by thinking about the early and late-time behavior of the reaction, and the spatial extents over which the reactants have traveled. At early times, each A or B has only had a chance to diffuse over a short distance, and on these spatial scales the reactant distribution still looks random. At long times, the distribution also looks random, as well, since the triangular power spectrum of the speckles shows us that these extra fluctuations are present over only a finite range of spatial frequency. (This can be seen most eas-

ily if a triangular function is plotted using a logarithmic x axis, in which case the curve will flatten at low spatial frequencies as the details of the beginning of the triangle are stretched out.) As a result, the late-time behavior closely follows the Zeldovich rate for initially random reactant distributions, since the reaction only “feels” randomness at later times. During the mid-time regime, though, the presence of extra long wavelength fluctuations due to the speckles slows the product formation rate, just as in the case of initially fractal distributions like those studied by Lindenberg *et al.* [6,7] (but over a finite extent for the speckles, whereas a real fractal has extra long wavelength fluctuations over an infinite extent).

In conclusion, we have successfully demonstrated a model experimental system for the nonclassical $A + B \rightarrow C$ reaction along with the effects of the initial reactant distribution. Our results also seem to show an experimental exhibition of the Zeldovich nonclassical rate behavior. Although more work would be necessary to measure the exact *reaction progress* slope over a longer period of time, contrasts between reactions initiated with homogenous illumination vs a speckled laser source show dramatically different kinetics, as a result of the strong dependence of the reaction behavior on its memory of the (speckled) initial conditions. These extreme qualitative differences would never appear in the classical case. These experiments demonstrate that the body of diffusion-limited, modern reaction kinetics results needs to be taken seriously, as even in this realistic case of a somewhat reversible reaction, the lack of mixing and the initial reactant distribution effects are dramatic.

ACKNOWLEDGMENTS

We acknowledge funding from the NSF Grant No. DMR9900434. Thanks go to Dr. Anna Lin for discussions of reaction kinetics concepts and results, as well as Matlab routines. We also thank Dr. Susan Barker and Dr. Heather Clark for their experience with fluorescent sensor molecules. Also, Dr. Andrea Stout’s input was invaluable when assessing dye behavior artifacts.

- [1] C. Kittel, *Introduction to Solid State Physics*, 3rd ed. (Wiley, New York, 1967).
- [2] Proceedings of the NiH meeting on Models of Non-Classical Reaction Rates, edited by G. Weiss, special issue of *J. Stat. Phys.* **65**, Nos. 5-6 (1991).
- [3] A.A. Ovchinnikov and Y.B. Zeldovich, *Chem. Phys.* **28**, 215 (1978).
- [4] D. Toussaint and F. Wilczek, *J. Chem. Phys.* **78**, 2642 (1983).
- [5] For geminate initial distributions, where A and B are landed (at $t=0$) as nearest neighbor pairs, $\alpha=d/2$ for $d \leq 2$ and $\alpha=1$ for $d \geq 2$ [4].
- [6] K. Lindenberg, P. Argyrakis, and R. Kopelman, in *Noise and Order: The New Synthesis*, edited by M. Millonas (Springer, New York, 1996), Chap. 12, pp. 171–203.
- [7] K. Lindenberg, A.H. Romero, and J.M. Sancho, *Int. J. Bifurcation Chaos Appl. Sci. Eng.* **8**, 853 (1998).
- [8] P. Argyrakis and R. Kopelman, *J. Phys. Chem.* **93**, 225 (1989).
- [9] E. Monson and R. Kopelman, *Phys. Rev. Lett.* **85**, 666 (2000).
- [10] E.E. Monson, Ph.D. dissertation, University of Michigan, 1999.
- [11] L. Galfi and Z. Racz, *Phys. Rev. A* **38**, 3151 (1988).
- [12] A. Yen, Y.E.L. Koo, and R. Kopelman, *Phys. Rev. E* **54**, 2447 (1996).
- [13] H. Taitelbaum, B. Vilensky, A.A. Lin, A.D. Yen, Y.E.L. Koo, and R. Kopelman, *Phys. Rev. Lett.* **77**, 1640 (1996).
- [14] B.J. Schwartz, J.C. King, J.Z. Zhang, and C.B. Harris, *Chem. Phys. Lett.* **203**, 503 (1993).
- [15] J.W. Goodman, in *Laser Speckle and Related Phenomena*, edited by J. C. Dainty (Springer-Verlag, New York, 1975), pp. 9–75.
- [16] M. Sjudahl, *Opt. Lasers Eng.* **29**, 125 (1998).
- [17] J. Walker, G. Reid, J. McCray, and D. Trentham, *J. Am. Chem. Soc.* **110**, 7170 (1988).

- [18] Fiber temporal stretching of the UV pulses has been neglected since the pulses are quite long (10 ns) and the absorption cross section changes only slightly with the time scale of excitation; see Ref. [17].
- [19] The experimental setup limits distortions of the speckle pattern by the capillary since the $n = 1.48$ capillary is surrounded by and contains $n = 1.33$ water. But, we make no specific claims about the details of the speckle pattern (e.g., size of speckles or lack of distortion to the pattern). The physical origins of this type of interference effect, though, should always lead to the formation of a speckled structure in all three dimensions, even if it is not completely symmetric in each dimension due to said distortions.
- [20] G. Zumofen, A. Blumen, and J. Klafter, *J. Chem. Phys.* **82**, 3198 (1985).
- [21] K.R. Delaney and R.S. Zucker, *J. Physiol. (London)* **426**, 473 (1990).
- [22] G.C.R. Ellis-Davies, J.H. Kaplan, and R.J. Barsotti, *Biophys. J.* **70**, 1006 (1996).
- [23] A.L. Escobar, P. Velez, A.M. Kim, F. Cifuentes, M. Fill, and J.L. Vergara, *Pfluegers Arch.* **434**, 615 (1997).
- [24] J.H. Kaplan and G.C.R. Ellis-Davies, *Biophys. J.* **53**, A36 (1988).
- [25] J.A. McCray, N. Fidlerlim, G.C.R. Ellis-Davies, and J.H. Kaplan, *Biochemistry* **31**, 8856 (1992).
- [26] G.C.R. Ellis-Davies, *Biophys. J.* **72**, WPME6 (1997).
- [27] G.C.R. Ellis-Davies and J.H. Kaplan, *Biophys. J.* **66**, A4 (1994).
- [28] G.C.R. Ellis-Davies and J.H. Kaplan, *Proc. Natl. Acad. Sci. U.S.A.* **91**, 187 (1994).
- [29] M. Eberhard and P. Erne, *Biochem. Biophys. Res. Commun.* **180**, 209 (1991).
- [30] M. Probes, Product Information Sheet MP 3010, Molecular Probes, Inc., 1996.
- [31] M. Eberhard and P. Erne, *Biochem. Biophys. Res. Commun.* **163**, 309 (1989).
- [32] J.P.Y. Kao and R.Y. Tsien, *Biophys. J.* **53**, 635 (1988).
- [33] F.A. Lattanzio, *Biochem. Biophys. Res. Commun.* **171**, 102 (1990).
- [34] F.A. Lattanzio and D.K. Bartschat, *Biochem. Biophys. Res. Commun.* **177**, 184 (1991).
- [35] G.L. Smith and D.J. Miller, *Biochim. Biophys. Acta* **839**, 287 (1985).
- [36] R.Y. Tsien and T. Pozzan, *Methods Enzymol.* **172**, 230 (1989).
- [37] M.D. Zhao, S. Hollingworth, and S.M. Baylor, *Biophys. J.* **70**, 896 (1996).
- [38] R.Y. Tsien, *Biochemistry-US* **19**, 2396 (1980).
- [39] BAPTA denotes 1, 2-bis (*o*-aminophenoxy) ethane-*N,N,N',N'*-tetraacetic acid. EDTA denotes ethylenediamine tetraacetic acid. EGTA denotes [Ethylenebis-(oxyethylenenitrilo)]-tetraacetic acid.
- [40] D.M. Bers and S.M. Harrison, *J. Physiol. (London)* **386**, P58 (1987).
- [41] S.M. Harrison and D.M. Bers, *Biochim. Biophys. Acta* **925**, 133 (1987).
- [42] P. Argyrakis, R. Kopelman, and K. Lindenberg, *Chem. Phys.* **177**, 693 (1993).
- [43] D.M. Bers, *Am. J. Physiol.* **242**, C404 (1982).
- [44] K. Sasaki, Z.Y. Shi, R. Kopelman, and H. Masuhara, *Chem. Lett.* **141**, 2 (1996).
- [45] R.J. Hunter, in *Zeta Potential in Colloid Science: Principles and Applications* (Academic Press, New York, 1988).
- [46] N. Periasamy, S. Bicknese, and A.S. Verkman, *Biophys. J.* **70**, MP345 (1996).
- [47] A.L. Stout and D. Axelrod, *Photochem. Photobiol.* **62**, 239 (1995).
- [48] B. Bock, M. Hilchenbach, K. Schauenstein, and G. Wick, *J. Histochem. Cytochem.* **33**, 699 (1985).
- [49] G.D. Johnson, R.S. Davidson, K.C. McNamee, G. Russell, D. Goodwin, and E.J. Holborow, *J. Immunol. Methods* **55**, 231 (1982).
- [50] G.D. Johnson and G.M.d.C. Nogueira Araujo, *J. Immunol. Methods* **43**, 349 (1981).
- [51] K. Valnes and P. Brandtzaeg, *J. Histochem. Cytochem.* **33**, 755 (1985).
- [52] A.L. Lin, E. Monson, and R. Kopelman, *Phys. Rev. E* **56**, 1561 (1997).
- [53] J.C. Dainty, *Opt. Acta* **17**, 761 (1970).